Contents lists available at ScienceDirect

Applied Catalysis B: Environmental

Switching of semiconducting behavior from n-type to p-type induced high photocatalytic NO removal activity in g-C$_3$N$_4$

Jianmin Luo [a,b,c], Guohui Dong [a,d,*], Yunqing Zhu [d], Zhong Yang [c], Chuanyi Wang [a,*]

[a] Laboratory of Environmental Sciences and Technology, Xinjiang Technical Institute of Physics & Chemistry, Key Laboratory of Functional Materials and Devices for Special Environments, Chinese Academy of Sciences, Urumqi 830011, China
[b] The Graduate School of Chinese Academy of Science, Beijing, 100049, China
[c] Xinjiang Uygur Autonomous Region Academy of Instrument Analysis, Urumqi 830011,China
[d] School of Environmental Science and Engineering, Shaanxi University of Science and Technology, Xian 710021, China

ARTICLE INFO

ABSTRACT

The utilization of photocatalytic technology to remove air pollutants has attracted global interest. However, it still suffers from low removal activities under visible light irradiation. In this study, we demonstrated that the switching of the semiconducting behavior from n-type to p-type can efficiently improve the photocatalytic activity of g-C$_3$N$_4$ for nitric oxide (NO) removal about 3.5 times. This is due to that such switching could change the majority of carriers in g-C$_3$N$_4$ from electrons to holes. Interestingly, the photocatalytic removal of NO in both n-type and p-type g-C$_3$N$_4$ is proceeded via hole oxidation. More importantly, p-type g-C$_3$N$_4$ displays strong stability in both photocatalytic performance and crystal structures. This study provides a new strategy to improve the photocatalytic activity of semiconductors for air pollution removal.

© 2017 Elsevier B.V. All rights reserved.

1. Introduction

The rapid development in economy leads to increasing demand for fossil fuels in our society [1]. In this situation, two important issues have become increasingly important. One is energy shortage since fossil fuels are finite and can only be exploited for a limited number of years [2]. The other is air pollution as a result of the combustion of fossil fuels [3]. As solar energy is inexhaustible and clean, the utilization of photocatalytic technologies to remove air pollutants has attracted worldwide interest [4]. Thus, over the past decades, various photocatalysts such as TiO$_2$ [5,6], CdS [7–11], BiOX (X = Cl, Br, I, or CO$_3$) [12–19], and SrTiO$_3$ [20–22] have been developed in an attempt to utilize solar energy for environmental purification and energy conversion. Among these developments, Wang et al. reported a metal-free graphitic carbon nitride (g-C$_3$N$_4$) semiconductor polymer [23]. This photocatalyst has the ability to produce hydrogen or oxygen via water splitting under visible light irradiation. Since then, g-C$_3$N$_4$ has become one of the hottest topics in photocatalysis owing to its high chemical stability, semiconductivity, special optical features, and simple preparation characteristics [24,25]. However, the photocatalytic activity of pure g-C$_3$N$_4$ still remains relative low because of the fast recombination of the photogenerated carriers [26]. To improve the efficiency of g-C$_3$N$_4$, various methods such as morphological modification, anionic or cationic doping, and coupling with other semiconductors have been developed [27–35]. Despite all these efforts, the visible light photocatalytic activity of g-C$_3$N$_4$ still remains low. Therefore, more efficient methods to improve the visible light photocatalytic activity of g-C$_3$N$_4$ are highly desired.

According to previous reports, most air pollutants are photocatalytically removed through oxidation reactions [36]. Therefore, photogenerated holes are preferred over electrons in these processes. Holes are known to prevail over electrons as photogenerated carriers in p-type semiconductors [37]. This is because p-type semiconductor has an acceptor level, which could trap electrons from valence band of semiconductor. As a result, the number of holes in p-type semiconductor is much bigger than that of electrons. Thus, it is reasonable to speculate that p-type semiconductors are more suitable for the photocatalytic removal of air pollutants as compared to their n-type counterparts. However, most existing p-type semiconductors such as NiO and Cu$_2$O typically present low shallow VB potentials (ca. 0.3–0.5 V) that limit the oxidation per-

* Corresponding authors at: Laboratory of Environmental Sciences and Technology, Xinjiang Technical Institute of Physics & Chemistry, Key Laboratory of Functional Materials and Devices for Special Environments, Chinese Academy of Sciences, Urumqi, 830011, China.
E-mail addresses: donggh@ms.xjb.ac.cn (G. Dong), cywang@ms.xjb.ac.cn (C. Wang).

formance of the photogenerated holes [38–40]. To overcome this limitation, it is desirable to develop new *p*-type semiconductors having high VB potential.

According to previous works, photogenerated holes from the valence band of g-C$_3$N$_4$ nanosheets with high oxidation potential (ca. 1.4 V) could oxidize most air pollutants [41]. Unfortunately, g-C$_3$N$_4$ shows *n*-type electrical conductivity [42]. A limited number of publications have shown that the semiconducting behavior of one semiconductor can be reversed via ion doping [43]. Thus, the semiconducting behavior of g-C$_3$N$_4$ nanosheets could be reversed from *n*-type to *p*-type such that photogenerated holes having high oxidation ability would be the prevalent carrier species, thus resulting in higher air pollution removal photocatalytic activities for *p*-type g-C$_3$N$_4$ nanosheets. Therefore, it is highly interesting to develop a simple method for switching the semiconducting behavior of g-C$_3$N$_4$ from *n*-type to *p*-type.

In this study, we synthesized *p*-type g-C$_3$N$_4$ nanosheets by filling the voids with chloride ions for the photocatalytic removal of NO under visible light. The detailed structure and photoreactivity of *p*-type g-C$_3$N$_4$ were investigated and compared with its counterpart, *n*-type one. Compared to *n*-type g-C$_3$N$_4$, *p*-type g-C$_3$N$_4$ demonstrated significantly higher photocatalytic efficiency for NO removal. The underline mechanisms of the semiconducting behavior switch and NO removal were deeply explored.

2. Experimental

2.1. Synthesis of carbon nitride photocatalysts

All chemicals were of analytical grade and were used without any further purification. *n*-type g-C$_3$N$_4$ nanosheets (N-g-C$_3$N$_4$) were synthesized through the following procedures. First, melamine (1 g) was mixed with cyanuric acid (2 g) in 20 mL of ethanol with constant stirring at 333 K to evaporate ethanol. The resultant mixture was placed in an alumina crucible provided with cover, and subsequently heated to 550 °C for 4 h in air to obtain the final sample. To prepare *p*-type g-C$_3$N$_4$ nanosheets (P-g-C$_3$N$_4$), 1 g of the as-prepared N-g-C$_3$N$_4$ was added to 100 mL of 0.1 mol/L HCl solution and stirred at 80 °C for 3 h. The resulting powder was collected by filtration, thoroughly washed with distilled water and ethanol, and finally oven-dried at 50 °C.

2.2. Characterization

X-ray diffraction (XRD) measurements were carried out on a Bruker D8 Advance diffractometer with monochromatized Cu Kα radiation (λ = 1.5406 Å). Transmission electron microscopy (TEM) images were obtained on a JEOL JSM-2010 microscope at an accelerating voltage of 200 kV. For TEM observation, the synthesized samples were dispersed in ethanol and subsequently dropped on lacey support film grids. X-ray photoelectron spectroscopy (XPS) measurements were carried out on a VG scientific ESCALAB Mark II spectrometer equipped with two ultra-high vacuum chambers. Nitrogen adsorption–desorption isotherms were carried out at 77 K on a Micrometrics ASAP2020 system after the samples were vacuum-dried at 180 °C overnight. The ultraviolet–visible (UV–vis) diffuse reflectance spectra (DRS) were obtained on a UV–vis spectrometer (Shimadzu UV-3600) with BaSO$_4$ as a reference and the reflection was converted into absorbance via the Kubelka–Munk method. The photoluminescence spectra (PL) of the samples were obtained on a fluorescence spectrometer (Hitachi F7000) at room temperature. The thermal stability of carbon nitride was tested on a thermal gravimetric analyzer (TGA, STA 449F3, Netzsch, Germany) at a heating rate of 10 °C min^{-1} from 30 to 800 °C under air atmosphere.

2.3. Photocatalytic activity tests

The photocatalytic activity of the resulting samples was investigated by performing photocatalytic NO removal experiments at ambient temperature in a continuous flow reactor. The volume of the reactor was 4.5 L (30 cm × 15 cm × 10 cm [L × W × H]) and was made of quartz glass. Before the NO removal experiment, one sample dish containing the appropriate photocatalysts was placed in the middle of the reactor. During the experiment, NO (10 ppm) was obtained from a compressed gas cylinder and subsequently diluted to ca. 600 ppb with an air stream supplied by a zero air generator. The mixture gas streams continuously passed through the reactor and the NOx analyzer (Thermo, 42i) with a flow rate of 1 L min^{-1}. A xenon lamp (λ > 420 nm, 14 W m^{-2}) was vertically placed outside the reactor above the sample dish. Before light irradiation, the mixture gas streams were continuously passed through the surface of photocatalyst to reach the adsorption–desorption equilibrium between the gases and the sample photocatalysts. Subsequently, the lamp was turned on to start the photocatalytic experiment. The concentration of NO was continuously measured using a chemiluminescence NO analyzer (Thermo, 42i). The NO removal efficiency (η) was calculated as follows:

$$\eta(\%) = (1 - C/C_0) \times 100\%$$

where C and C$_0$ are the concentrations of NO in the outlet and the feeding streams, respectively.

For the photocatalytic NO removal experiments, the sample dish was prepared as follows: 50 mg of photocatalyst was added to 10 mL of distilled H$_2$O and ultra-sonicated for 20 min. The aqueous suspension was subsequently coated into a glass dish with a diameter of 5 cm. Subsequently, this dish was placed in an oven at 60 °C until complete water removal.

3.1. Photoelectrochemical experiments

The photoelectrochemical experiments were conducted on a CHI660E workstation using a conventional three-electrode system. Indium tin oxide (ITO) glass which was loaded with 20 mg samples was chosen as work electrode; Standard calomel electrode and Pt slice (1 × 1 cm^2) were chosen as reference electrode and counter electrode, respectively. In experiment, three different electrodes were immersed in a 0.1 M KCl aqueous solution (electrolyte). When measure the photocurrent of different samples, a 300 W Xenon lamp equipped with a 420 nm optical filter was used as light source.

4. Results and discussion

The crystal structures of the final samples were examed by XRD (Fig. 1a). Both N-g-C$_3$N$_4$ and P-g-C$_3$N$_4$ samples show two peaks at ca.13.0° and 27.4° which are ascribed to the (100) and (002) crystal planes of g-C$_3$N$_4$, respectively. The small angle peak at ca. 13.0° arises from the in-plane structural packing motif of tri-s-triazine units, while the more intense peak at ca. 27.4° is the characteristic of interlayer stacking. Comparing with N-g-C$_3$N$_4$, the peak at 27.4° of P-g-C$_3$N$_4$ is more intense and shifts to higher 2θ values, suggesting a closer packing of the g-C$_3$N$_4$ interlayers. Moreover, the peak at ca. 13.0° of P-g-C$_3$N$_4$ is nearly negligible, indicating that HCl might have been incorporated into the structure with the resultant destruction of the order of the tri-s-triazine units packing motif. The incorporation of chloride ions in P-g-C$_3$N$_4$ is also proved by elemental mapping images. As shown in Fig. 1b and f, chloride ions are evenly distributed on the surface of P-g-C$_3$N$_4$. On the contrary, no chloride ions appear on the surface of N-g-C$_3$N$_4$ (Fig. 1c). Fig. 2 shows TEM images of the N-g-C$_3$N$_4$ and P-g-C$_3$N$_4$ samples. As can be seen from the images, both N-g-C$_3$N$_4$ and P-g-C$_3$N$_4$ are
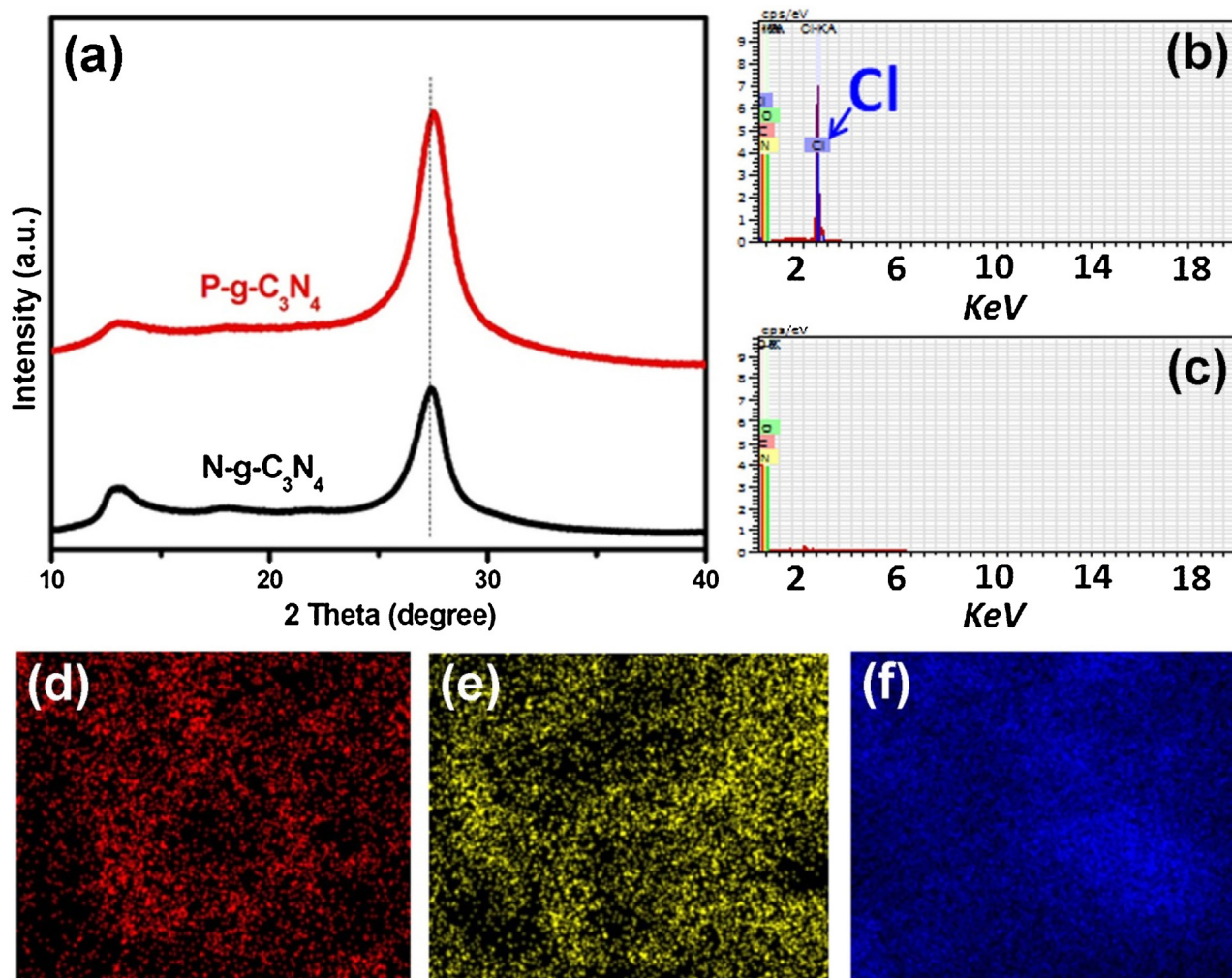
Fig. 1. XRD patterns of P-g-C_3N_4 and N-g-C_3N_4 samples (a); EDS spectrum of P-g-C_3N_4 (b) and P-g-C_3N_4 (c); Elemental mapping of P-g-C_3N_4 for C element (d), N element (e), Cl element (f).
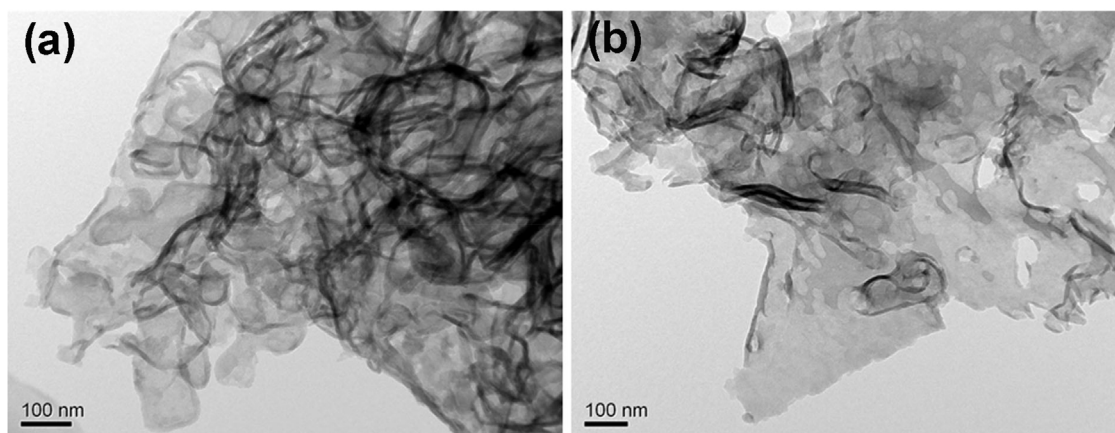

Fig. 2. TEM images of N-g-C_3N_4 (a); P-g-C_3N_4 (b) samples.

composed of ultra-thin (10 nm thickness) nanosheets (Fig. 2). Such ultrathin structure favors the homogeneous distribution of HCl within g-C_3N_4 because there is footy for the concentration gradient with depth.

XPS is an effective technique to determine surface elemental composition of samples. In this work, XPS measurements were car-ried out to confirm the incorporation of chloride ions into the final products. As shown in Fig. 3a, no XPS peaks corresponding to Cl species appear in N-g-C_3N_4. However, in the case of P-g-C_3N_4, a Cl 1s peak shows up (Fig. 3a), suggesting that chloride ions were incorporated into g-C_3N_4. With the aim to clarify the existence of chloride ions within P-g-C_3N_4, we investigated the change of
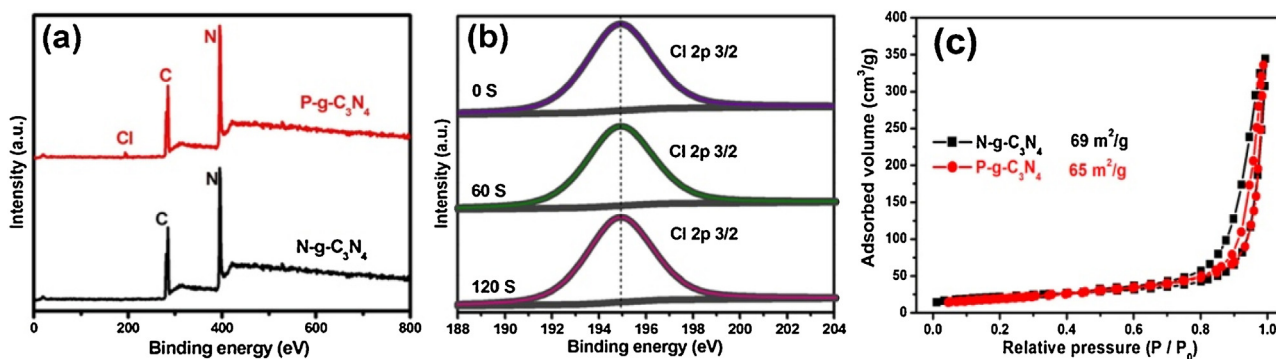
Fig. 3. (a) Survey XPS spectra of the sample P-g-C_3N_4 and N-g-C_3N_4; (b) the high-resolution Cl 2p XPS spectra of P-g-C_3N_4; (c) Nitrogen adsorption-desorption isotherms of different samples.

the high resolution Cl 1s XPS peak upon Ar$^+$ sputtering from 0 to 120s (Fig. 3b). The peak intensity of Cl 1s in P-g-C_3N_4 did not change during Ar$^+$ sputtering, implying that Cl ions were internally incorporated within the structure of P-g-C_3N_4. This may be benefited from the ultrathin structure. To investigate if the incorporated HCl could affect the specific surface area of g-C_3N_4, Nitrogen adsorption–desorption isotherms were employed to test the specific surface area of different samples. As shown in Fig. 3c, the specific surface area of P-g-C_3N_4 is 65 m^2/g. This value is only a little smaller than that of N-g-C_3N_4 (69 m^2/g), implying that the incorporation of HCl could not improve the specific surface area of g-C_3N_4.

In order to determine whether HCl was stable in P-g-C_3N_4, TGA was carried out to measure the changes in the weight of P-g-C_3N_4 and N-g-C_3N_4 as a function of temperature. As shown in Fig. 4a, heating under argon atmosphere resulted in an intense mass loss for both P-g-C_3N_4 and N-g-C_3N_4 in the temperature range of ca. 550–760 °C, which could be attributed to thermal decomposition of g-C_3N_4. P-g-C_3N_4 showed a lower mass loss as compared to N-g-C_3N_4, suggesting the formation of resolved g-C_3N_4 to a lesser extent during the thermal condensation of P-g-C_3N_4. This is understandable when considering the incorporation of HCl into P-g-C_3N_4 which accounts for a certain weight percentage. More importantly, unlike N-g-C_3N_4, an additional mass loss at ca. 398–487 °C occurs for P-g-C_3N_4. This additional mass loss could be attributed to the release of HCl and suggests that HCl is stable in P-g-C_3N_4 under the ambient temperature.

Mott–Schottky analysis was subsequently carried out to study the semiconducting behavior of the final samples. A straight line with a positive slope, the characteristic of n-type semiconductor behavior, was observed for N-g-C_3N_4 (Fig. 4b). In contrast, a linear relationship with a negative slope (i.e., p-type semiconducting behavior) was observed for P-g-C_3N_4 (Fig. 4c). Hence, the semiconducting behavior of g-C_3N_4 was successfully switched from n-type to p-type by a simple process. Since the only difference between N-g-C_3N_4 and P-g-C_3N_4 is the incorporation of HCl, the reversal of the semiconducting behavior can be attributed to the incorporated HCl. To clarify this point, the HCl was removed from P-g-C_3N_4 and its Mott–Schottky spectrum was compared with that of the original sample. In this work, a simple calcination (450 °C, 3 h) was used to remove the HCl from P-g-C_3N_4. As shown in Fig. 4d, the Cl 1s peaks disappear from the XPS pattern after HCl removal from P-g-C_3N_4, confirming that the calcination treatment is effective in removing the chlorine species. Mott–Schottky analysis was subsequently carried out to study the semiconducting behavior of the post-calcined sample. Remarkably, unlike the original sample, a Mott–Schottky spectrum with a positive slope was observed for the post-calcined P-g-C_3N_4 sample (Insert of Fig. 4c). Thus, the post-calcined sample shows an n-type semiconducting behavior, in good agreement with

the semiconducting behavior of g-C_3N_4. Therefore, the switching of the semiconducting behavior can be attributed to the incorporation of HCl.

To further prove this effect by the incorporated HCl, the band structures as well as the electron densities of N-g-C_3N_4 and P-g-C_3N_4 were simulated via the plane-wave pseudopotential approach based on the density functional theory. A model for P-g-C_3N_4 was built by inserting HCl into the voids of the g-C_3N_4 primitive cell (Fig. 5). The total density of states (DOS, Fig. 6a and b), conduction and valence band (CB and VB, respectively) structures diagram (Fig. 6c and d) of N-g-C_3N_4 and P-g-C_3N_4 are displayed in Fig. 6, respectively. Comparing with P-g-C_3N_4, a new band ascribed to the orbital Cl 2p appears above the VB of P-g-C_3N_4 (Fig. 6b and d). This new band can accept electrons from the VB of P-g-C_3N_4 acting as an acceptor level. As well known, acceptor level is the signature of p-type semiconductors. Thus, the simulation result further supports that the switching of the semiconducting behavior was produced by the incorporation of Cl●.

According to previous reports, an intermediate level might improve the visible light absorption efficiency, thereby favoring the electron excitation of the semiconductor [44]. Generally, the electron excitation in a semiconductor strongly depends on its light absorption ability and band gap energy. Therefore, UV–vis DRS (Fig. 7a) was employed to investigate the light absorption ability and band gap energy of the two samples. Compared with N-g-C_3N_4, a noticeable red shift appears for the intrinsic absorption edge of P-g-C_3N_4. Meanwhile, the band gaps of N-g-C_3N_4 and P-g-C_3N_4 are calculated to be ca. 2.89 and 2.73 eV (Fig. 7b), respectively. Moreover, the absorption of g-C_3N_4 has been extended from bluish violet range to entire visible region (Fig. 7a). The emerging absorption is because the acceptor level can accept electrons from the VB of P-g-C_3N_4. This means that the visible light with energy smaller than the band gap of P-g-C_3N_4 (2.73 eV) could also excite valence electrons (Fig. 7c). However, N-g-C_3N_4 can only be excited by the light with energy larger than its band gap (2.89 eV). Obviously, the acceptor level can improve the visible light absorption efficiency and favor electron excitation, indicating that P-g-C_3N_4 can produce photoinduced electrons and holes to a larger extent.

After the generation of electron–hole pairs, these species can follow two fates. These species can separate and trigger the subsequent chemical reactions. Alternatively, these species can recombine with each other. Previous work revealed that an intermediate level allows the transportation of photogenerated carriers [44], thereby inhibiting the recombination of the generated electron–hole pairs. It is reasonable to consider that the switching of the semiconducting behavior would improve the electrical conductivity of g-C_3N_4. To prove this hypothesis, we carried out electrochemical impedance spectroscopy (EIS) measurements to study the electrical conductivity of N-g-C_3N_4 and P-g-C_3N_4. As
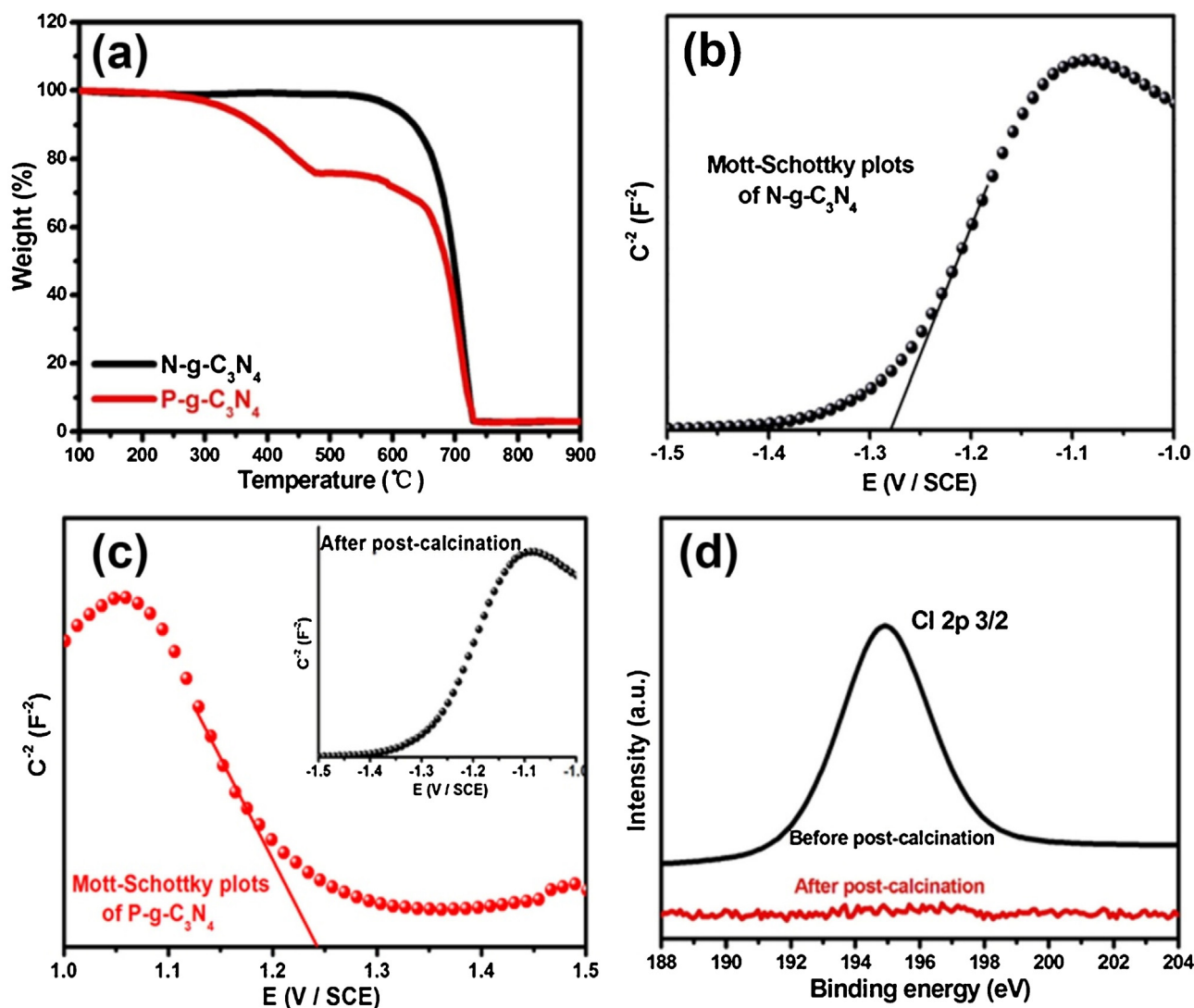
Fig. 4. TGA curves of N-g-C_3N_4 and P-g-C_3N_4 (a); Mott-Schottky plot of N-g-C_3N_4 (b), P-g-C_3N_4 (c) and post-calcinated P-g-C_3N_4 (insert of c); the high-resolution Cl 2p spectra of P-g-C_3N_4 before and after post-calcination (d).

shown in Fig. 8a, the Nyquist plots diameter of P-g-C_3N_4 is significantly lower than that of N-g-C_3N_4, confirming that the switching of the semiconducting behavior from *n*-type to *p*-type increases the electrical conductivity as a result of the formation of an acceptor level.

Materials with high electrical conductivity have good separation of their photogenerated carriers. From this prospect, PL measurements were performed to study the separation of the photogenerated electrons and holes in N-g-C_3N_4 and P-g-C_3N_4. Fig. 8b displays the PL spectra of the two samples at room temperature. The strong emission peak of N-g-C_3N_4 at ca. 455 nm is derived from the direct recombination of electrons and holes from the transition band. In contrast, the weaker intensity of the PL peak of P-g-C_3N_4 confirms the higher separation and transfer efficiency of its photogenerated carriers. Therefore, the switching of the semiconducting behavior of g-C_3N_4 favors the absorption of visible light and the separation of the photogenerated carriers, eventually producing more holes and electrons for the photoredox reaction. This large concentration of photogenerated carriers can be confirmed by photocurrent measurements. As shown in Fig. 8c, the photocatalyst electrode prepared from N-g-C_3N_4 shows anodic photocurrent under visible light irradiation, thereby confirming the *n*-type semiconductor character of N-g-C_3N_4. However, it is worth mentioning

that a cathodic photocurrent is provided by the photocatalyst electrode prepared from P-g-C_3N_4. This cathodic photocurrent is a clear indication of the *p*-type semiconductor character of this sample, in good agreement with the results of the Mott–Schottky analysis. Moreover, P-g-C_3N_4 generates significantly higher photocurrent as compared to N-g-C_3N_4, thereby confirming that P-g-C_3N_4 could produce larger amount of photoinduced carriers.

Besides the concentration of photoinduced carriers, the photocatalytic activity of a semiconductor is also related to the redox properties of the photoinduced carriers, which ultimately depend on the VB and CB potentials. Fig. 8d presents the XPS valence band spectra of N-g-C_3N_4 and P-g-C_3N_4. As can be seen from the images, both samples show similar edges of the VB maximum energy, demonstrating the oxidation ability of the holes in the VB is not affected by the reversion of the semiconducting behavior.

Nitric oxide (NO) is a common gaseous pollutant producing environmental problems such as acid rain, haze, photochemical smog, and ozone depletion [45]. Meanwhile, the concentration of this dangerous gas in the atmosphere is increasing year by year [46]. Therefore, the removal of this gas from the atmosphere is crucial and necessary for meeting our Green Earth Plan. In this work, the photocatalytic activities of the as-prepared N-g-C_3N_4 and P-g-C_3N_4 samples were explored by measuring the NO photocatalytic
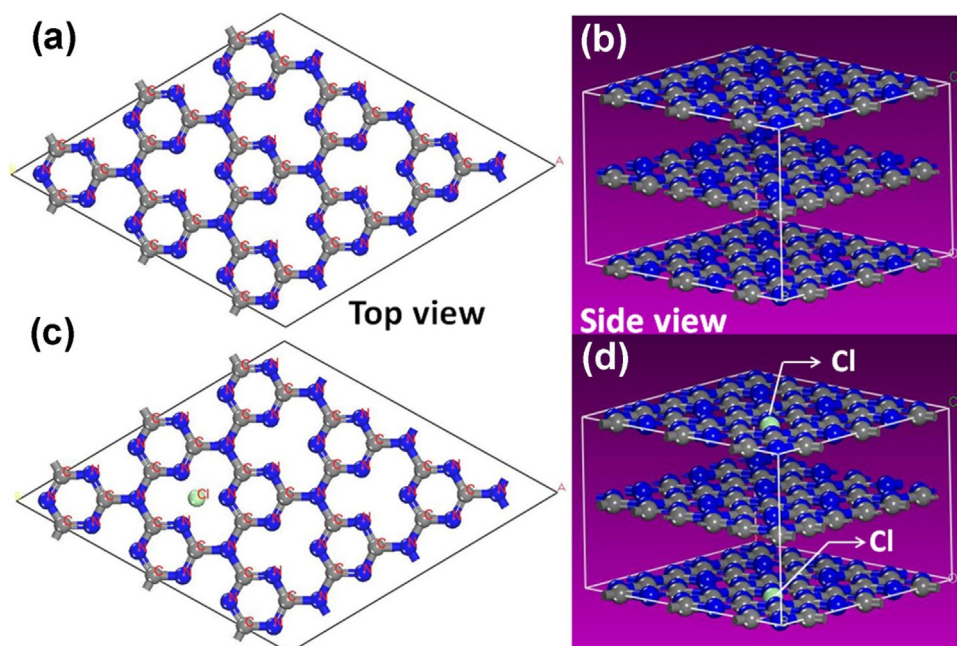
Fig. 5. The crystal model of N-g-C$_3$N$_4$ (a,b) and P-g-C$_3$N$_4$ (c.d).
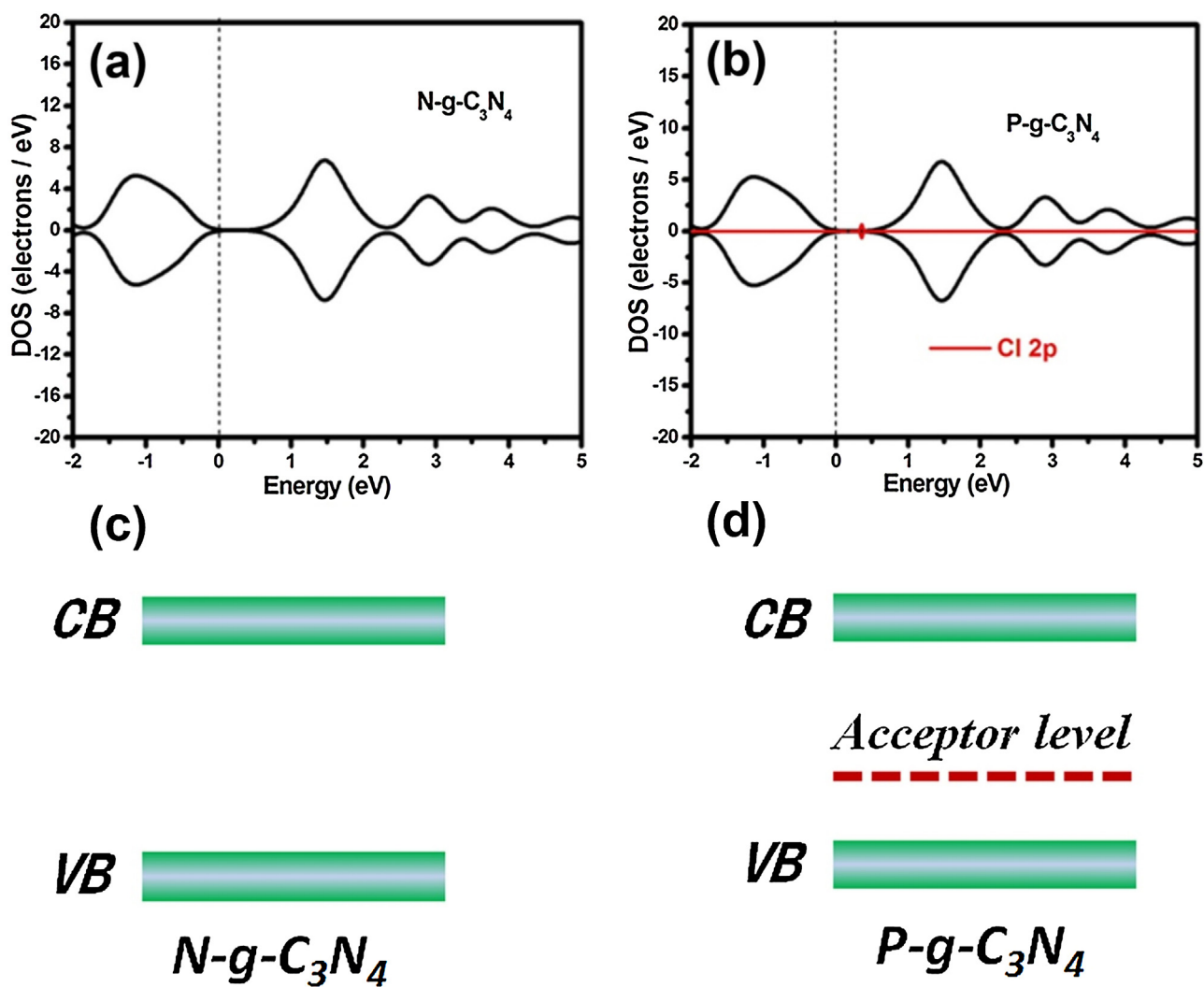
Fig. 6. The total density of states (DOS) of N-g-C$_3$N$_4$ (a) and P-g-C$_3$N$_4$ (b); the band structure diagram of N-g-C$_3$N$_4$ (c) and P-g-C$_3$N$_4$ (d).
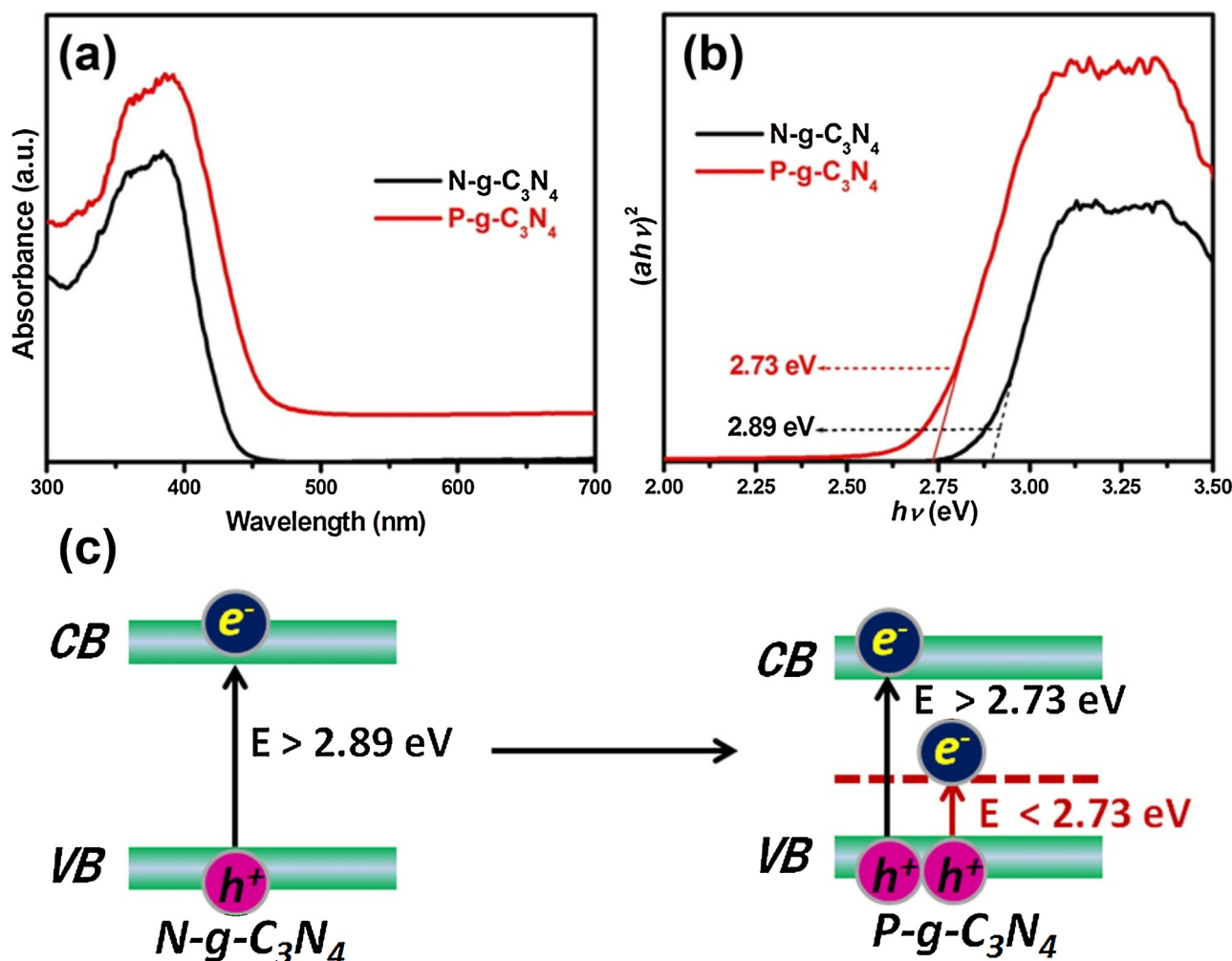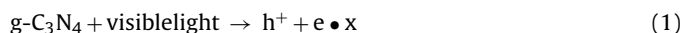
Fig. 7. UV–vis absorption spectra (a), transformed diffuse reflectance spectra (b) of N-g-C_3N_4 and P-g-C_3N_4 samples; the excitation diagram of N-g-C_3N_4 and P-g-C_3N_4 samples (c).

removal under visible light irradiation ($\lambda > 420$ nm). As shown in Fig. 9a, direct photolysis of NO is negligible in the absence of photocatalyst, indicating the high photostability of NO under visible light irradiation. When N-g-C_3N_4 was used as a catalyst, 43% of the initial NO was removed after 45 min of irradiation (0.8% min^{-1}), while P-g-C_3N_4 removed 80% in only 30 min under similar irradiation conditions (2.8% min^{-1}). The NO removal result clearly evinces that the switching of the semiconducting behavior from *n*-type to *p*-type can efficiently improve the photocatalytic activity of g-C_3N_4 for nitric oxide (NO) removal about 3.5 times. Besides the measurement of NO decrease, we also detected the concentration changes of NO_2 and noted that the main products of NO removal over both N-g-C_3N_4 and P-g-C_3N_4 were NO_2 (Fig. 9b). Although NO_2 is a toxic product, it can be absorbed by H_2O or alkali liquor (e.g. $2NO_2 + 2NaOH = NaNO_3 + NaNO_2 + H_2O$) to form nitrates, which are good nitrogen fertilizer. Because NO is hard to be absorbed by H_2O or other kinds of liquor, the oxidation from NO to NO_2 is a significant NO removal process.

To further investigate whether the reversion of the semiconducting behavior would affect the photocatalytic removal pathway of NO, active species trapping experiments were carried out. In these trapping experiments, potassium iodide (KI) [41], potassium dichromate ($K_2Cr_2O_7$) [47], *tert*-butyl alcohol (TBA) [48], and *p*-benzoquinone (PBQ) [49] were selected to trap the photogenerated holes, electrons, hydroxide radical ($^{\bullet}OH$), and superoxide anion radical ($^{\bullet}O_2\bullet$) species, respectively. As shown in Fig. 10, addition of KI

significantly decreases the NO removal activity for both N-g-C_3N_4 and P-g-C_3N_4, suggesting that photogenerated holes play a critical role in NO removal for both samples. Conversely, the addition of $K_2Cr_2O_7$ can only cause little inhibition of NO removal. Considering that the photogenerated electrons can activate O_2 to produce active oxygen species such as $^{\bullet}OH$ and $^{\bullet}O_2\bullet$, it is essential to investigate the role of these active oxygen species in the NO removal process. The addition of TBA did not alter the NO removal rate for any of the samples, thereby indicating that $^{\bullet}OH$ is not involved in the photocatalytic removal of NO. Meanwhile, addition of PBQ slightly decreased the NO removal activity of both N-g-C_3N_4 and P-g-C_3N_4 samples, thereby suggesting that $^{\bullet}O_2\bullet$ is the main reason for role of electrons. Since both hole and $^{\bullet}O_2\bullet$ can in NO removal for both samples, we concluded that the reversion of the semiconducting behavior did not affect the pathway or mechanism of NO removal at g-C_3N_4. The photocatalytic removal of NO over both N-g-C_3N_4 and P-g-C_3N_4 may involve the following reactions, Eq. (1)–(4),

$$g\text{-}C_3N_4 + visiblelight \rightarrow h^+ + e \bullet x \tag{1}$$

$$2h^+ + NO + H_2O \rightarrow NO_2 + 2H^+ \tag{2}$$

$$e \bullet + O_2 \rightarrow {}^{\bullet}O_2\bullet \tag{3}$$

$$NO + {}^{\bullet}O_2\bullet \rightarrow NO_3\bullet \tag{4}$$

Though the pathway and mechanism of NO removal have not been changed, the switching of the semiconducting behavior from

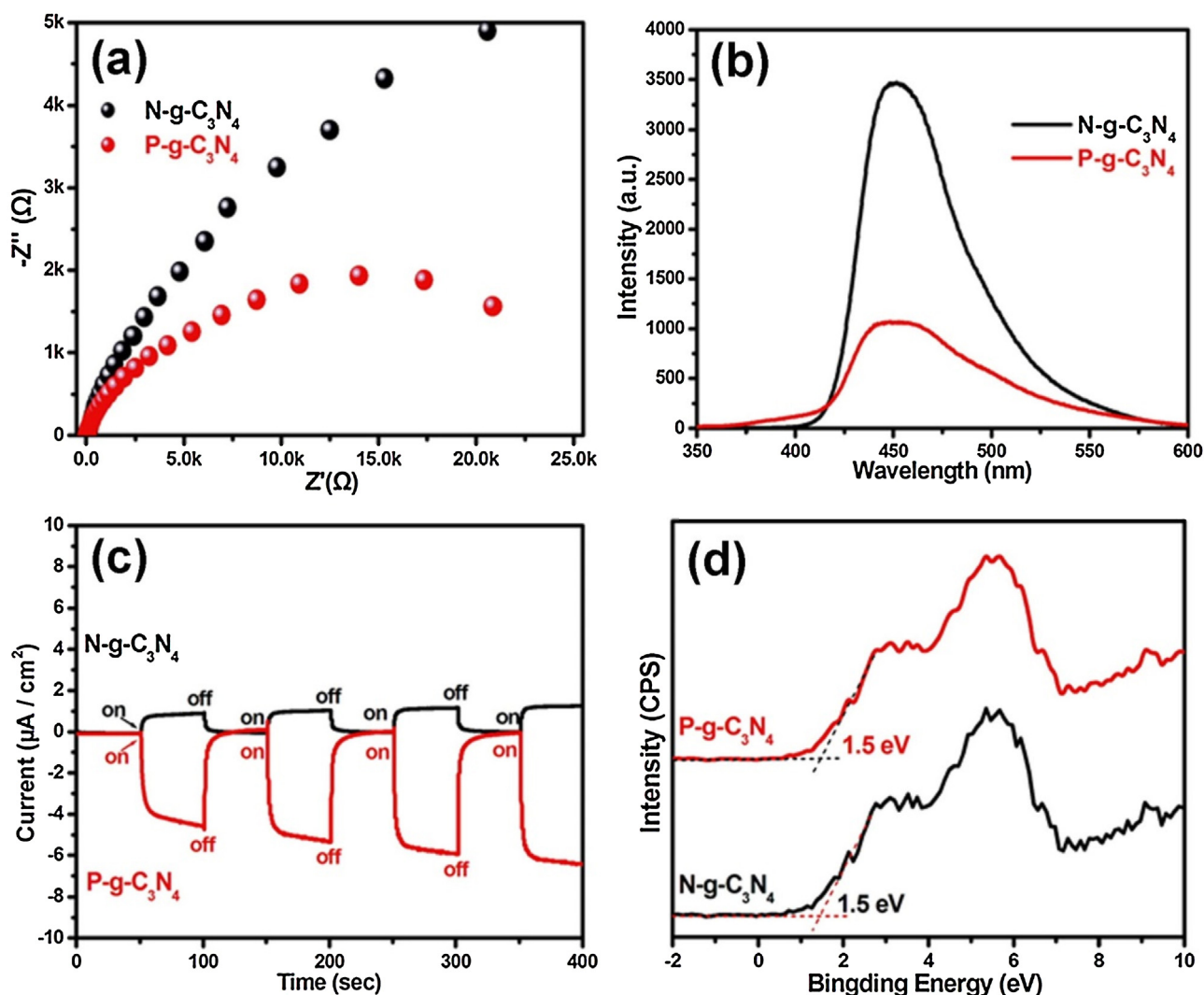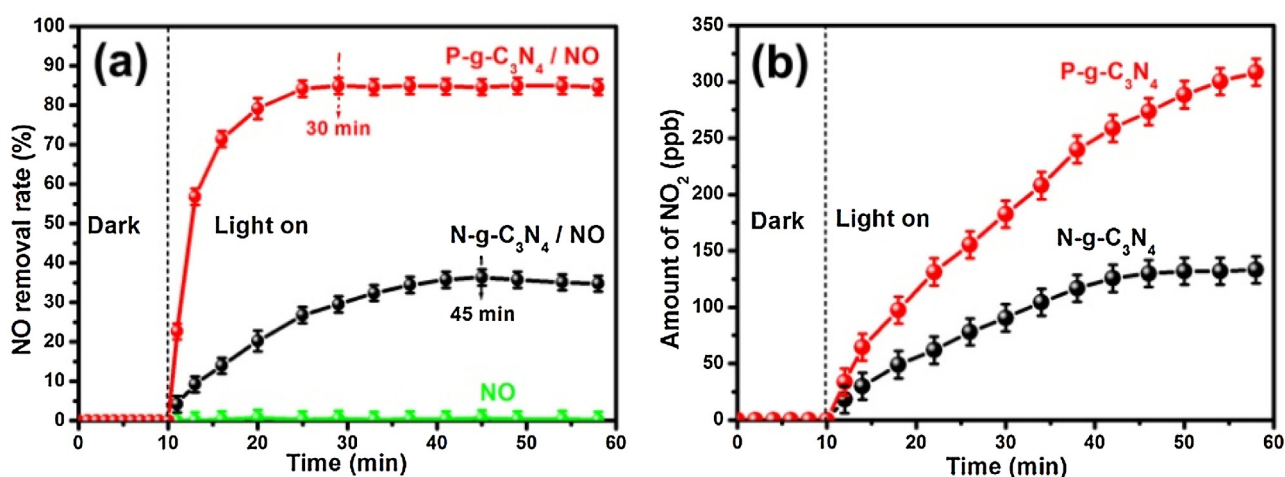**Fig. 8.** Nyquist Plot (a), PL spectra (b), Current-time curves (c) and XPS valence band spectra (d) of N-g-C$_3$N$_4$ and P-g-C$_3$N$_4$.

Fig. 9. (a) Relative change in NO concentration (C/C$_0$) as a function of irradiation time tested over P-g-C$_3$N$_4$ and N-g-C$_3$N$_4$; (b) NO$_2$ concentration changing with irradiation time tested over P-g-C$_3$N$_4$ and N-g-C$_3$N$_4$.

n-type to *p*-type can efficiently improve the photocatalytic activity of g-C$_3$N$_4$ for nitric oxide (NO) removal about 3.5 times. This improvement was mainly benefited from the acceptor level which can improve the visible light absorption efficiency and favor electron excitation. As shown in Fig. 7a, the absorption of g-C$_3$N$_4$ has been extended from bluish violet range to entire visible region. The emerging absorption is because the new acceptor level can accept electrons from the VB of P-g-C$_3$N$_4$. This means that the
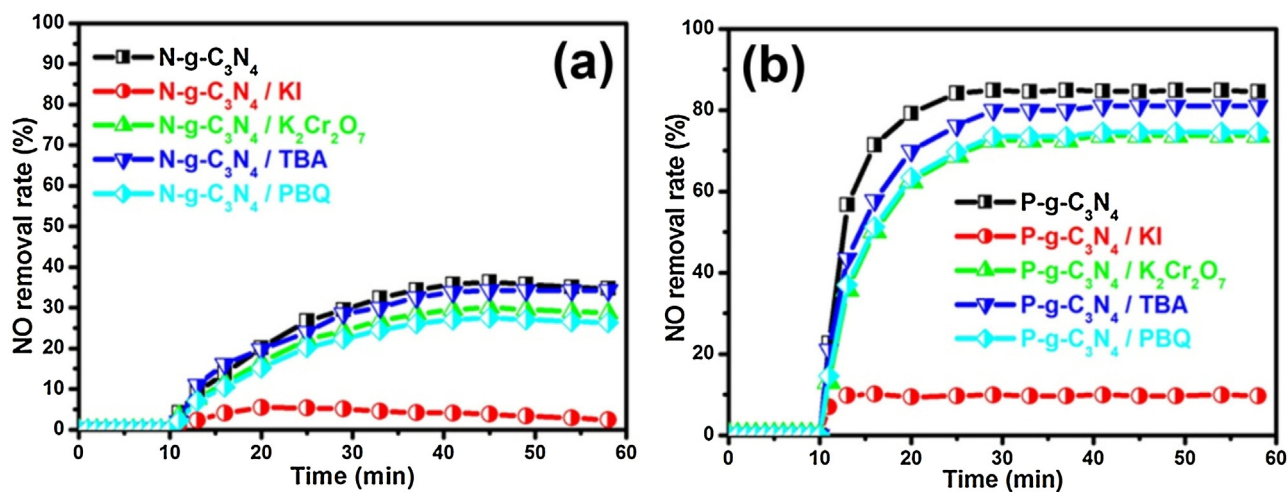
Fig. 10. Comparison of photocatalytic activities of N-g-C$_3$N$_4$ (a) and P-g-C$_3$N$_4$ (b) in different photocatalysis systems under visible light irradiation ($\lambda > 420$ nm).
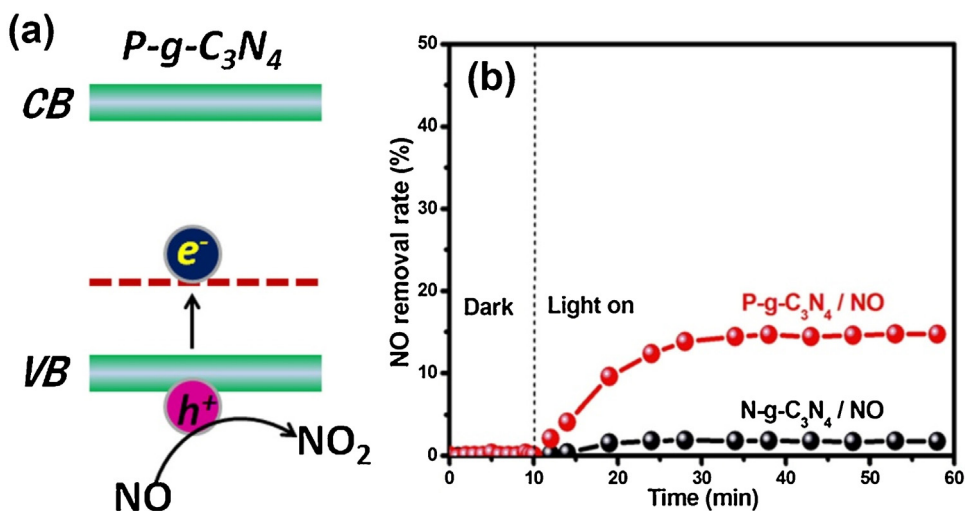

Fig. 11. The low energy excitation diagram of P-g-C$_3$N$_4$ (a); Photocatalytic removal of NO in the presence N-g-C$_3$N$_4$ and P-g-C$_3$N$_4$ under the LED lamp irradiation ($\lambda = 550$ nm) (b).
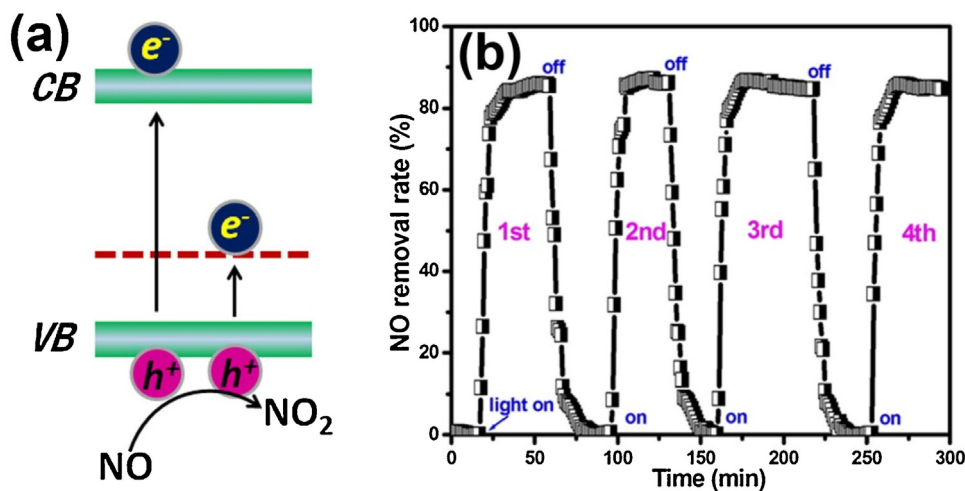

Fig. 12. The excitation diagram of P-g-C$_3$N$_4$ samples (a); The stability of P-g-C$_3$N$_4$ sample in multiple runs of NO removal (b).

visible light with energy smaller than that of band gap P-g-C$_3$N$_4$ (2.73 eV) could also excite valence electrons and produce photogenerated holes to oxidize NO (Fig. 11a). To confirm this speculation, we repeat the photocatalytic NO removal experiments using the 550 nm LED lamp instead xenon lamp. It is very interesting to notice that the NO removal over P-g-C$_3$N$_4$ attain the value of 15%, while very weak removal occurs on N-g-C$_3$N$_4$ (Fig. 11b), confirming that P-g-C$_3$N$_4$ could oxidize NO under the low energy light irradiation. It is well known that only the light with the wavelength less than 460 nm could excite g-C$_3$N$_4$ to produce photogenerated holes. However, the P-g-C$_3$N$_4$ that we synthesized can be excited by the light with energy lower than its band gap (Fig. 12a). This feature makes P-g-C$_3$N$_4$ have more application potential in the removal of air pollutants.

Furthermore, the stability of P-g-C$_3$N$_4$ after multiple cycles of NO photooxidation was evaluated by comparing its activity as well as crystal structure before and after the recycling test. As shown in Fig. 12b, the photocatalytic activity and crystal structure of P-g-C$_3$N$_4$ remain nearly unchanged after the recycling test, indicating that P-g-C$_3$N$_4$ is very stable during photocatalysis.

6. Conclusion

In conclusion, we have experimentally and theoretically demonstrated that the incorporation of HCl in g-C$_3$N$_4$ can switch the semiconducting behavior of g-C$_3$N$_4$ nanosheets from *n*-type to *p*-type, where the incorporated Cl• formed an acceptor level above the VB. This new formed intermediate level improves the visible light absorption efficiency while favors electron excitation and suppresses the recombination of the photogenerated carriers of g-C$_3$N$_4$. Therefore, *p*-type g-C$_3$N$_4$ produces photogenerated carriers to a larger extent for subsequent redox reaction. In *p*-type semiconductors, photogenerated holes prevail over electron carriers. Meanwhile, the switching of the semiconducting behavior does not decrease the oxidation ability of holes in the VB of g-C$_3$N$_4$. As a result, *p*-type g-C$_3$N$_4$ displays a higher activity in photooxidation NO removal than its *n*-type counterpart. This study provides a new strategy to improve the photooxidation NO removal activity of g-C$_3$N$_4$, and also paves the way for switching the semiconducting behavior of other semiconductors.

References

[1] D. Kim, K.K. Sakimoto, D.C. Hong, P.D. Yang, Artificial photosynthesis for sustainable fuel and chemical production, Angew. Chem. Int. Ed. 54 (2015) 2–10.
[2] N. Armaroli, B. Vincenzo, Solar electricity and solar fuels: status and perspectives in the context of the energy transition, Chem.-Eur. J. 22 (2016) 32–57.
[3] Z. Liu, D. Guan, W. Wei, S. Davis, P. Ciais, J. Bai, S. Peng, Q. Zhang, K. Hubacek, G. Marland, R. Andris, D. Brown, J. Lin, H. Zhao, C. Hong, T. Boden, K. Feng, G. Peters, F. Xi, J. Liu, Y. Li, Y. Zhao, N. Zeng, K. He, Reduced carbon emission estimates from fossil fuel combustion and cement production in China, Nature 524 (2015) 335–338.
[4] D. Spasiano, R. Marotta, S. Malato, P.F. Ibañez, I.D. Somma, Solar photocatalysis: materials reactors, some commercial, and pre-industrialized applications. A comprehensive approach, Appl. Catal. B: Environ. 170–171 (2015) 90–123.
[5] I. Vukoje, T. Kovac, J. Dzunuzovic, E. Dzunuzovic, D. Loncarevic, S.P. Ahrenkiel, J.M. Nedeljkovic, Photocatalytic ability of visible-light-responsive TiO$_2$ nanoparticles, J. Phys. Chem. C 120 (2016) 18560–18569.
[6] S. Pal, A.M. Laera, A. Licciulli, M. Catalano, A. Taurino, Biphase TiO$_2$ microspheres with enhanced photocatalytic activity, Ind. Eng. Chem. Res. 53 (2014) 7931–7938.
[7] W.T. Yao, S.H. Yu, S.J. Liu, J.P. Chen, X.M. Liu, F.Q. Li, Architectural control syntheses of CdS and CdSe nanoflowers branched nanowires, and nanotrees via a solvothermal approach in a mixed solution and their photocatalytic property, J. Phys. Chem. B 110 (2006) 11704–11710.
[8] S. Xiong, B. Xi, Y. Qian, CdS hierarchical nanostructures with tunable morphologies: preparation and photocatalytic properties, J. Phys. Chem. C 114 (2010) 14029–14035.
[9] M. Muruganandham, Y. Kusumoto, C. Okamoto, A. Muruganandham, M. Abdulla-Al-Mamun, B. Ahmmad, Mineralizer-assisted shape-controlled synthesis characterization, and photocatalytic evaluation of CdS microcrystals, J. Phys. Chem. C 113 (2009) 19506–19517.
[10] K. Prasad, M. Ashokkumar, Photocatalytic properties of CdS nanoparticles synthesized under various ultrasonic operating conditions, Ind. Eng. Chem. Res. 53 (2014) 715–722.
[11] X. Wang, M. Liu, Z. Zhou, L. Guo, Toward facet engineering of CdS nanocrystals and their shape-dependent photocatalytic activities, J. Phys. Chem. C 119 (2015) 20555–20560.
[12] L. Sun, L. Xiang, X. Zhao, C.J. Jia, J. Yang, Z. Jin, X. Cheng, W. Fan, Enhanced visible-light photocatalytic activity of BiOI/BiOCl heterojunctions: key role of crystal facet combination, ACS Catal. 5 (2015) 3540–3551.
[13] H. Huang, X. Han, X. Li, S. Wang, P.K. Chu, Y. Zhang, Fabrication of multiple heterojunctions with tunable visible-light-active photocatalytic reactivity in BiOBr–BiOI full-range composites based on microstructure modulation and band structures, ACS Appl. Mater. Interfaces 7 (2015) 482–492.
[14] M. Li, J. Zhang, H. Gao, F. Li, S.E. Lindquist, N. Wu, R. Wang, Microsized BiOCl square nanosheets as ultraviolet photodetectors and photocatalysts, ACS Appl. Mater. Interfaces 8 (2016) 6662–6668.
[15] F. Tian, H. Zhao, Z. Dai, G. Cheng, R. Chen, Mediation of valence band maximum of BiOI by Cl incorporation for improved oxidation power in photocatalysis, Ind. Eng. Chem. Res. 55 (2016) 4969–4978.
[16] H. Feng, Z. Xu, L. Wang, Y. Yu, D. Mitchell, D. Cui, X. Xu, J. Shi, T. Sannomiya, Y. Du, W. Hao, S.X. Dou, Modulation of photocatalytic properties by strain in 2D BiOBr nanosheets, ACS Appl. Mater. Interfaces 7 (2015) 27592–27596.
[17] H. Li, J. Shang, H. Zhu, Z. Yang, Z. Ai, L. Zhang, Oxygen vacancy structure associated photocatalytic water oxidation of BiOCl, ACS Catal. 6 (2016) 8276–8285.
[18] J. Zhang, F. Shi, J. Lin, D. Chen, J. Gao, Z. Huang, X. Ding, C. Tang, Self-assembled 3-D architectures of BiOBr as a visible light-driven photocatalyst, Chem. Mater. 20 (2008) 2937–2941.
[19] J.X. Xia, S. Yin, H. Li, H.M. Xu, Y.S. Yan, Q. Zhang, Self-assembly and enhanced photocatalytic properties of BiOI hollow microspheres via a reactable ionic liquid, Langmuir 27 (2011) 1200–1206.
[20] S. Ouyang, P. Li, H. Xu, H. Tong, L.Q. Liu, J. Ye, Bifunctional-nanotemplate assisted synthesis of nanoporous SrTiO$_3$ photocatalysts toward efficient degradation of organic pollutant, ACS Appl. Mater. Interfaces 6 (2014) 22726–22732.
[21] B. Modak, S.K. Ghosh, Enhancement of visible light photocatalytic activity of SrTiO$_3$: a hybrid density functional study, J. Phys. Chem. C 119 (2015) 23503–23514.
[22] Q. Kuang, S. Yang, Template synthesis of single-crystal-like porous SrTiO$_3$ nanocube assemblies and their enhanced photocatalytic hydrogen evolution, ACS Appl. Mater. Interfaces 5 (2013) 3683–3690.
[23] X.C. Wang, K. Maeda, A. Thomas, K. Takanabe, G. Xin, J.M. Carlsson, K. Domen, M. Antonietti, A metal-free polymeric photocatalyst for hydrogen production from water under visible light, Nat. Mater. 8 (2009) 76–80.
[24] Y. Zheng, L.H. Lin, B. Wang, X.C. Wang, Graphitic carbon nitride polymers toward sustainable photoredoxcatalysis, Angew. Chem. Int. Ed. 54 (2015) 12868–12884.
[25] T. Xiong, W.L. Cen, Y.X. Zhang, F. Dong, Bridging the g-C$_3$N$_4$ interlayers for enhanced photocatalysis, ACS Catal. 6 (2016) 2462–2472.
[26] J.G. Yu, S. Wang, J. Low, W. Xiao, Enhanced photocatalytic performance of direct Z-scheme g-C$_3$N$_4$–TiO$_2$ photocatalysts for the decomposition of formaldehyde in air, Phys. Chem. Chem. Phys 15 (2013) 16883–16890.
[27] C.S. Pan, J. Xu, Y.J. Wang, D. Li, Y.F. Zhu, Dramatic activity of C$_3$N$_4$/BiPO$_4$ photocatalyst with core/shell structure formed by self-assembly, Adv. Funct. Mater 22 (2012) 1518–1524.
[28] J.Y. Zhang, Y.H. Wang, J. Jin, J. Zhang, Z. Lin, F. Huang, J.G. Yu, Efficient visible-light photocatalytic hydrogen evolution and enhanced photostability of core/shell CdS/g-C$_3$N$_4$ nanowires, ACS Appl. Mater. Interfaces 5 (2013) 10317–101324.
[29] G.H. Dong, K. Zhao, L.Z. Zhang, Carbon self-doping induced high electronic conductivity and photoreactivity of g-C$_3$N$_4$, Chem. Commun. 48 (2012) 6178–6180.
[30] Y.J. Zhang, T. Mori, J.H. Ye, M. Antonietti, Phosphorus-doped carbon nitride solid: enhanced electrical conductivity and photocurrent generation, J. Am. Chem. Soc. 132 (2010) 6294–6295.
[31] Y.B. Li, H.M. Zhang, P. Liu, D. Wang, Y. Li, H.J. Zhao, Cross-linked g-C$_3$N$_4$/rGO nanocomposites with tunable band structure and enhanced visible light photocatalytic activity, Small 9 (2013) 3336–3344.
[32] S.C. Yan, Z.S. Li, Z.G. Zou, Photodegradation of rhodamine B and methyl orange over boron-doped g-C$_3$N$_4$ under visible light irradiation, Langmuir 26 (2010) 3894–3901.

[33] G. Liu, P. Niu, C.H. Sun, S.C. Smith, Z.G. Chen, Unique electronic structure induced high photoreactivity of sulfur-doped graphitic C_3N_4, J. Am. Chem. Soc. 132 (2010) 11642–11648.

[34] H.F. Shi, G.Q. Chen, C.L. Zhang, Z.G. Zou, Polymeric g-C_3N_4 coupled with $NaNbO_3$ nanowires toward enhanced photocatalytic reduction of CO_2 into renewable fuel, ACS Catal. 4 (2014) 3637–3643.

[35] G.H. Dong, Z.H. Ai, L.Z. Zhang, Efficient anoxic pollutant removal with oxygen functionalized graphitic carbon nitride under visible light, RSC Adv. 4 (2014) 5553–5560.

[36] Q.L. Yu, H.J. Brouwers, Z. Zhang, Indoor air purification using heterogeneous photocatalytic oxidation. Part I: experimental study, Appl. Catal. B: Environ. 92 (2009) 454–461.

[37] F. Odobel, L.L. Pleux, Y. Pellegrin, E. Blbat, New photovoltaic devices based on the sensitization of p-type semiconductors: challenges and opportunities, Acc. Chem. Res. 43 (2010) 1063–1071.

[38] Z. Zhang, C. Shao, X. Li, C. Wang, M. Zhang, Y. Liu, Electrospun nanofibers of p-type NiO/n-type ZnO heterojunctions with enhanced photocatalytic activity, ACS Appl. Mater. Interfaces 2 (2010) 2915–2923.

[39] H. Xu, W. Wang, W. Zhu, Shape evolution and size-controllable synthesis of Cu_2O octahedra and their morphology-dependent photocatalytic properties, J. Phys. Chem. B 110 (2006) 13829–13834.

[40] Z. Zheng, B. Huang, Z. Wang, M. Guo, X. Qin, X. Zhang, P. Wang, Y. Dai, Crystal faces of Cu_2O and their stabilities in photocatalytic reactions, J. Phys. Chem. C 113 (2009) 14448–14453.

[41] G.H. Dong, W.K. Ho, Y.H. Li, L.Z. Zhang, Facile synthesis of porous graphene-like carbon nitride ($C_6N_9H_3$) with excellent photocatalytic activity for NO removal, Appl. Catal. B: Environ. 174–175 (2015) 477–485.

[42] Y. Hou, Z. Wen, S. Cui, X. Guo, J. Chen, Constructing 2D porous graphitic C_3N_4 nanosheets/nitrogen-doped graphene/layered MoS_2 ternary nanojunction with enhanced photoelectrochemical activity, Adv. Mater. 25 (2013) 6291–6297.

[43] J.C. Yu, G. Jia, K. Wing, T. Zi, Z. Li, Effects of F• doping on the photocatalytic activity and microstructures of nanocrystalline TiO_2 powders, Chem. Mater. 14 (2002) 3808–3816.

[44] M.J. Yuan, O. Voznyy, D. Zhitomirsky, P. Kanjanaboos, E. Sargent, Synergistic doping of fullerene electron transport layer and colloidal quantum dot solids enhances solar cell performance, Adv. Mater. 27 (2015) 917–921.

[45] Z.Y. Wang, Y. Huang, W.K. Ho, J.J. Cao, Z.X. Shen, S.C. Lee, Fabrication of $Bi_2O_2CO_3$/g-C_3N_4 heterojunctions for efficiently photocatalytic NO in air removal: in-situ self-sacrificial synthesis characterizations and mechanistic study, Appl. Catal. B: Environ. 199 (2016) 123–133.

[46] G.H. Dong, W.K. Ho, L.Z. Zhang, Photocatalytic NO removal on BiOI surface: the change from nonselective oxidation to selective oxidation, Appl. Catal. B: Environ. 168–169 (2015) 490–496.

[47] C.H. Kim, G.S. Qi, K. Dahlberg, W. Li, Strontium-doped perovskites rival platinum catalysts for treating NO_x in simulated diesel exhaust, Science 327 (2010) 1624–1627.

[48] L. Wang, X.Z. Jiang, Plasma-induced reduction of chromium (VI) in an aqueous solution, Environ. Sci. Technol. 42 (2008) 8492–8497.

[49] G.H. Dong, L.P. Yang, F. Wang, L. Zang, C.Y. Wang, Removal of nitric oxide through visible light photocatalysis by g-C_3N_4 modified with perylene imides, ACS Catal. 6 (2016) 6511–6519.